



Supplementary Materials for

Low Mid-Proterozoic Atmospheric Oxygen Levels and the Delayed Rise of Animals

Noah J. Planavsky, Christopher T. Reinhard, Xiangli Wang,
Danielle Thomson, Peter McGoldrick, Robert T. Rainbird, Thomas Johnson, Woodward Fischer,
and Timothy W. Lyons

correspondence to: noah.planavsky@yale.edu; chris.reinhard@eas.gatech.edu

This PDF file includes:

Materials and Methods
Supplementary Text
Figs. S1 to S5
Table S1
References (33-106)

Other Supplementary Materials for this manuscript includes the following:

Databases S1 to S2: [Database S1. Sample and geochemical information,
Database S2, Laser ablation data]

Materials and Methods

Methods

Our method for Cr isotopes is based on Ref. 19. Briefly, an acid split from a multi-acid digest containing 1 μg Cr was mixed with a certain amount of ^{50}Cr - ^{54}Cr spike for a constant spike/sample ratio ($^{54}\text{Cr}_{\text{spike}}/^{52}\text{Cr}_{\text{sample}} \approx 0.5$). After drying down, samples were dissolved in 0.25 ml 1N HCl and then diluted to 9 ml with nanopure water. One milliliter of 0.2 M $(\text{NH}_4)_2\text{S}_2\text{O}_8$ was added to all samples, and the solutions were heated for two hours at $\sim 130^\circ\text{C}$ to oxidize Cr(III) to Cr(VI). After cooling, the solutions were loaded directly onto 2 ml AG1x8 (100-200 mesh) anion exchange resin pre-cleaned with distilled 5N HNO_3 and 6 N HCl and preconditioned with 0.025 N HCl. Matrix elements were eluted with 0.2 N and 2 N HCl. Cr(VI) on the resin was reduced and released from the anion exchange resin by 2 N HNO_3 with 2 wt% H_2O_2 . After drying down, samples were dissolved in 6 N HCl and passed through 0.2 ml AG1x8 (100-200 mesh) resin preconditioned with 6 N HCl to remove Fe, which forms an anionic complex. After drying down, samples were treated with 100% HNO_3 to destroy residual organic matter from the resin. Chromium isotopic composition was measured with a Nu Plasma MC-ICP-MS at University of Illinois at Urbana-Champaign. Chromium isotope data were collected in 5 blocks, 10 cycles per block, and 5 seconds integration per cycle. The double spike method also gave precise concentrations for all samples. Each set of three samples was bracketed by unprocessed NIST 979 standards and sample values were normalized to the bracketing standards. A NIST SRM 3112a standard and a blank were processed with samples through the same procedure. Processed NIST SRM 3112a gave the same isotopic composition as the unprocessed split within error. Blank Cr levels in each batch were monitored for and found to be negligible compared to the Cr in samples. The external precision based on 11 duplicate analyses of processed NIST SRM 3112a standard and 16 duplicate samples is $< \pm 0.1\%$ (2σ). Cr isotopic compositions are reported using conventional δ notation relative to the NIST 979 standard:

$$\delta^{53}\text{Cr}(\text{‰}) = \left[\frac{\left(\frac{^{53}\text{Cr}}{^{52}\text{Cr}} \right)_{\text{sample}}}{\left(\frac{^{53}\text{Cr}}{^{52}\text{Cr}} \right)_{\text{standard}}} - 1 \right] \cdot 1000 \quad .$$

Laser ablation work was done at CODES, University of Tasmania following the procedure outlined by Ref. 33. Representative examples of the Proterozoic iron formations were analyzed by laser ablation inductively coupled mass spectrometry (LA-ICP-MS) at CODES, University of Tasmania. We used a New Wave 213-nm solid-state laser microprobe coupled to an Agilent 7500ce quadrupole ICP-MS to perform quantitative spot analyses and produce qualitative image maps of trace element distributions (Figure S1). Ablations were carried out in a small volume cell purged with pure He. The resulting ablation aerosol was mixed with Ar prior to introduction to the ICPMS torch. Details of instrument optimization and laser conditions can be found in Ref. 33. Quantitative trace element data were obtained by ablating spots (50 μm or 22 μm diameter) and using Fe as an internal standard. An ‘in-house’ fused glass standard (GSD-1G) was used for quantification. This glass standard has been optimized for trace element analysis of oxides and calibrated against two well-characterized synthetic glasses: NIST

612 and STDGL2b2. The utilized quantification approach has been previously described for analysis using STDGL2b2 standard (33). Analytical errors due to matrix-dependent laser-induced fractionation were < 15% for examined trace elements, and were propagated into calculated Cr/Ti values according to:

$$\frac{\delta R}{R} = \sqrt{\left(\frac{\delta x}{x}\right)^2 + \left(\frac{\delta y}{y}\right)^2} \quad ,$$

where " δ " terms denote absolute error, x and y denote the measured concentrations of Cr and Ti, and R is the calculated Cr/Ti ratio.

For electron microscopy, we used a FEI XL-30 Environmental Scanning Electron Microscope (ESEM) operated under high vacuum setting at Yale University and a ZEISS 1550 VP FESEM, equipped with a Robinson-type BSE detectors and an Oxford X-ray Energy Dispersive Spectrometer (EDS) system at Caltech. Electron microprobe analyses were performed on a JEOL JXA-8200 at Caltech. Representative thin sections were coated with a layer of carbon 15 nm thick, and then studied with wavelength-dispersive spectroscopy using the JEOL JXA-8200 Electron Probe Micro-analyzer at Caltech using a current of 200 nA, voltage of 15 kV, and counting time of 80 ms per pixel.

Materials

Our Phanerozoic ironstones come from the University of Cincinnati museum collection. Information on each sample is available in the museum database using the provided repository numbers. These samples were previously the target of a microprobe study (34). The University of Cincinnati samples were supplemented with samples from the Red Mountain Formation, given that this unit has been extensively studied and is considered a 'type' ironstone deposit (35). Precambrian ironstones were newly collected for this study. We provide information about the geologic setting of the Mesoproterozoic and Neoproterozoic units below, which provide the focus of the study. Information about the Archean and early Proterozoic units targeted—the Sinqeni Formation and Timeball Hill Formation—is provide in Refs. 36-37. Splits of samples will be archived at the Yale Peabody Museum. It is important to note that ironstone units are typically found over relatively limited stratigraphic intervals. However, we sampled the largest available stratigraphic range and, more importantly, as wide a range of representative facies as possible (see Figure S1). Modern mudstones data in Fig. 1 is from Ref. 38.

Measurements were made from either bulk powders or isolated grains. Where present, secondary veins (e.g., late stage calcite veins) were avoided by picking from crushed chips at 10-20 times magnification. Probe quality thin sections were made for all of the samples except for the Timeball Hill Formation and Red Mountain Formation, where only thin sections from representative samples were made. After reflected light petrography, thin section were examined at the SEM facilities at Department of Geology and Geophysics at Yale University or the Division of Geological and Planetary Sciences at Caltech. Representative samples were also selected for microprobe and laser ablation work (14 samples; see above).

Ironstones

Given the broad lithologic similarity it has been proposed the term ‘ironstone’ be abandoned, but use of term has persisted for Phanerozoic and Precambrian units and the term does have some descriptive value (39). We use the term ‘ironstone’ to refer to shallow water iron-rich sedimentary deposits that experienced significant sedimentary reworking during deposition. In our sample suite the ironstones are typically granular and in most cases oolitic. Ooidal ironstones were historically referred to as Minette (Europe) or Clinton (USA)-type iron deposits. Lithologically these deposits share some similarity with Archean and Proterozoic granular iron formations, although the depositional environments and modes of formation of these two sedimentary rock types differ. Importantly, ironstones present a lithofacies that occurs in both Proterozoic and Phanerozoic strata—typical iron formation does not—and thereby presents a good archive from which to compare the Cr isotope systematics across a broad interval of Earth history.

Most ironstones used in this study occur in distinct condensed horizons within siliciclastic deltaic and nearshore marine deposits. In Phanerozoic time, these littoral environments typically contain benthic fauna. Ironstones typically occur within a predictable sequence stratigraphic setting marked by a transition from black shale at the base of the succession, to gray shale and siltstone, then to sandstones, and finally to sandstones and oolitic ironstones with cross-stratification. Within the ironstones, reduced iron phases are typically found in offshore facies, with oxidized facies dominating in more nearshore environments (35). Ironstones are typically considered to be condensed deposits and to have been deposited within the maximum flooding interval (35), and are often ascribed to accumulation in flooded cratonic and intracratonic basins or foreland basins.

The petrogenesis of ironstones is still imperfectly understood, however the Amazon delta provides insight into the processes likely responsible for typical ironstone deposition (22). In the Amazon, extensive early diagenetic iron cycling and steady physical reworking promote accumulation of iron-rich sediments with extremely high Fe/S ratios (22). Reworking of iron-rich pedogenic clasts in shallow marine environments is typically invoked to explain ironstone iron enrichments; however hydrothermal iron sources have also been invoked. Our samples were deposited in high energy, shallow-water settings and were not deposited in proximity to any known hydrothermal centers (more below). Thus we infer that the source of the iron was provided by local or regional crustal weathering with the transport of hydrothermal iron to these shallow water depositional systems being highly unlikely. Besides showing clear differences in their Cr isotope composition, Phanerozoic ironstones, relative to mid-Proterozoic ironstones, are more enriched in the redox sensitive element V (and to a lesser extent U). We tentatively link this increase in V enrichments to greater V mobilization and more efficient V transport under more oxidized surface conditions in the Phanerozoic.

The 1.7 Ga Chuanlinggou Formation, Changcheng Group

The Chuanlinggou Formation was deposited in the Yanshan Basin, a continental rift that developed on the northern margin of the North China Block around 1.8 Ga. The Changcheng Group is the first sedimentary interval in the basin and consists of the Changzhougou, Chuanlinggou, Tuanshanzi, and Dahongyu Formations. The minimum age of deposition comes from zircon U-Pb ages of 1625 ± 6 Ma (40) and 1625.9 ± 8.9 Ma (41) from overlying Dahongyu volcanic rocks in the Jixian area. Recently, the age model for the deposition of sedimentary strata within the Changcheng Group was refined to 1.7-1.6 Ga with U-Pb volcanic ages of 1673 ± 10 Ma for a granite-porphry dike (42) and 1731 ± 4 Ma for a mafic dike (43). These dikes emplaced into the Archean metamorphic basement but are unconformably overlain by the Changzhougou Formation in the Beijing area.

Samples for this study come from the Jixian area. In this region, the Changzhougou is characterized by coarse sandstones and conglomerates that are fluvial or shallow marine in origin. The Changzhougou Formation grades into the lower Chuanlinggou Formation, which consists mainly of silty shale with interbedded sandstones, representing a littoral-intertidal marine environment. The middle-upper Chuanlinggou Formation is composed of black shales of subtidal to lagoonal origin with frequent intercalations of intertidal sandstone and dolostone. The ironstones are found in the lower part of the Chuanlinggou Formation, with iron-rich grains being found over roughly 20 meters of section. The ironstone member contains three main facies: oolitic, stromatolitic, and granular. All three facies contain interbedded sandstones. The iron mineralogy of the member is dominated by hematite, but pyrite and siderite are present in the parts of the oolitic facies. The stromatolites form cm-scale columns and have been interpreted as having a microbial influence on formation. The granular facies contain medium sand-sized hematite grains lacking internal structure whereas the oolitic facies contain coarse sand-sized coated grains typically interspersed with finer quartz sand grains.

The ca. 1.65 Ga Freedom Formation

The Freedom Formation in the Midwest of the USA lies conformably above the Seeley Slate, which is above the Baraboo Quartzite (44). The Freedom Formation is at its maximum 300 meters thick and includes ferruginous shales, ferruginous cherts, and iron-rich dolostones. The lower half of the formation consists mainly of thinly bedded slates and cherts and lesser dolomite, as well as localized bodies of granular hematite-rich intervals. The upper half of the formation is predominantly dolomitic shales. The mineralogy is relatively simple with the unit containing only quartz, dolomite, hematite, magnetite, and chlorite. The Baraboo Quartzite and Seeley Slate are both supermature sedimentary units deposited in a shallow marine environment adjacent to a rhyolitic/granitic landmass that had undergone intense and sustained tropical weathering (44). The youngest detrital zircons in the Baraboo Quartzite are 1710 Ma, providing a maximum age for the underlying unit (44). There are no direct constraints on the ages of the overlying units nor on the timing of regional metamorphism and folding. It has been suggested folding of the sedimentary succession occurred at ca. 1630 Ma (45). Therefore,

there are large uncertainties on the minimum age of the unit and additional geochronological work is needed. However, available age constraints do indicate a mid-Proterozoic age. We have tentatively assigned an age of 1.67 Ga to the unit.

Samples for this study come from drill core from the Cahoon Iron Mine on the south limb of the Baraboo syncline about 3 km northwest of Devils Lake State Park, which is housed at a core repository of the Wisconsin Geological and Natural History Survey (WGNHS). The core shale is composed of silt-shale and ironstone facies. There are mm-cm scale layers of quartz, magnetite, and lesser carbonate grains. The magnetite and hematite occur predominantly as mm-scale granules that lack the conspicuous layering that would suggest an ooid precursor.

The 1.45 Ga Sherwin Ironstone, Roper Group

The Sherwin ironstone is a member of the Roper Group in Northern Australia. The Roper Group is found over an area of 145,000 km² and is typically several thousand meters thick. The succession was deposited in an intracratonic setting with several connected sub-basins and, therefore, it has been referred to as the Roper Superbasin. The Roper sedimentary succession consists of formal formations and undifferentiated groups (46). The broader tectonic context for the superbasin is poorly resolved, but there must have been active subsidence to allow for over 5,000 meters of deposition in the epicenter of some sub-basins. The ironstone member is found in the lower part of the McMinn Formation, the maximum age of which is based on a single zircon U-Pb age of 1492 ± 4 Ma from the underlying lower Mainoru Formation (47). The minimum age is poorly constrained and is based on a Rb-Sr age of 1429 ± 31 Ma in Kyalla Member of the McMinn Formation (48).

The McMinn Formation directly overlies the Velkerri Formation, which is characterized by deepwater black shale facies. The lowest part of the McMinn Formation contains a high-energy sandstone referred to as the Moroak Member (46). This grades conformably into the Sherwin Ironstone Member, which consists of crudely bedded to trough cross-stratified sandstones and iron ooids. The ferruginous facies is hematite dominated, but chamosite and siderite are present in parts. The iron ooid layer is up to 5 meters thick but is laterally discontinuous, with the iron-rich intervals concentrated in thin lenses. The sandstone and iron ooid facies grades into deeper water mud and siltstones inferred to be deposited on a storm dominated shelf. Our ironstone samples come from recent diamond drill cores (Sherwin Iron), with the exception of pisolitic ironstones, which come from trenches or cliff facies. Given the relatively narrow stratigraphic range of the ironstone member we took samples from a broad geographic range and the full range of facies.

The 0.9 Ga to 0.75 Ga Shaler Supergroup

The Aok ironstone and the Wynniatt Formation are part of the Tonian to Cryogenian Shaler Supergroup (~1100 – 723 Ma). The Shaler Supergroup is a > 4-km-thick sedimentary succession composed of shallow-marine carbonate rocks, sandstones, shales and evaporites deposited in the Amundsen Basin, which developed after the assembly of Rodinia (49). The maximum age of the Shaler comes from a detrital zircon dated to 1151

Ma (50). The minimum age is $723 \pm 4/-2$ Ma based on U-Pb geochronology of diabase sills that intrude the sedimentary succession and feed overlying flood basalts, part of the Franklin Large Igneous Province (51). There are three Re-Os depositional ages of 892 ± 13 Ma from the Boot Inlet Formation above the Aok Formation, 849 ± 48 Ma for the Black Shale Member of the lower Wynniatt Formation, and 761 ± 41 Ma for the Upper Carbonate Member of the Wynniatt Formation. The Strata have experienced only low-grade metamorphism, except in immediate proximity to diabase sills (26).

The Aok formation is a thin shallow water succession dominated by carbonates and sandstones, bracketed by two thicker shallow marine formations dominated by fluvial sandstones—the underling Nelson Head Formation and the overlying Grassy Bay Formation. The Grassy Bay Formation also contains finer-grained siliciclastics. The iron rich horizon, for which the formation is named, is approximately two meters thick. The Wynniatt Formation is approximately a kilometer higher in the succession. Interpreted as a storm-dominated carbonate ramp, the formation is divided into four informal members: (1) Lower Carbonate member, an upward-deepening succession of supra- to sub-tidal carbonate rocks; (2) Black Shale member, a recessive interval of dark-grey siltstone and silty shale deposited in a pro-delta setting; (3) Stromatolitic Carbonate member, comprising stacked upward-shallowing cycles of subtidal to supratidal carbonate rocks; and (4) Upper Carbonate member, an upward-shallowing succession from subtidal black calcareous shale to peritidal, cross-bedded intraclastic grainstone and stromatolitic limestone (52). Our shale samples come from the Upper Carbonate member. Based on available ages and chemostratigraphic constraints we interpret the age of the shale unit to be between 800 Ma and 740 Ma.

Supplementary Text

A kinetic framework for Cr(III) and Mn(II) oxidation

Under the conditions that typically pertain to oxygenated surface waters Cr(III) is thermodynamically unstable and the speciation of Cr should be dominated by Cr(VI) (53, 54). However, the kinetics of Cr(III) oxidation by O_2 are extremely slow in natural settings (55, 56). As a result, the most common oxidant for Cr(III) in Earth surface environments is Mn, in the form of Mn(III,IV) (hydr)oxides (15, 57-61). The kinetics of this process can be generally formulated as (62-65):

$$-\frac{d[\text{Cr(III)}]}{dt} = \frac{d[\text{Cr(VI)}]}{dt} \approx k[\text{Cr(III)}]^a [\text{MnO}_x]^b \quad ,$$

where k is a rate constant, MnO_x denotes some representation of Mn-oxide concentration or surface site availability and a/b denote constants that reflect the order of the reaction with respect to Cr(III) and MnO_x species.

Here, we employ the following rate law for Cr(III) oxidation with manganite (63):

$$\frac{d[\text{Cr(VI)}]}{dt} = k_*([\text{Cr(III)}]_0 - [\text{Cr(VI)}]_t)\{\gamma - \text{MnOOH}\} \quad ,$$

where k_* is the rate constant for the reaction, $[\text{Cr(III)}]_0$ represents the initial amount of Cr(III), $[\text{Cr(VI)}]_t$ represents the amount of Cr(VI) at time t , and $\{\gamma - \text{MnOOH}\}$ represents the surface site availability of MnOOH (in $\text{m}^2 \text{L}^{-1}$).

Rates of Mn(IV) production are formulated in one of two ways. The first, meant to represent biotic Mn(II) oxidation, is described according to a Michaelis-Menten-type expression (66-69) where it is assumed that O_2 is the limiting substrate:

$$\frac{d[\text{Mn(IV)}]}{dt} = \mu_{max} \frac{[\text{O}_2]}{K_{\text{O}_2} + [\text{O}_2]} .$$

Here, μ_{max} represents the maximum turnover rate of Mn-oxidizing microorganisms, K_{O_2} represents the half-saturation constant for microbial metabolism of O_2 , and $[\text{O}_2]$ represents the ambient concentration of dissolved oxygen. The latter is imposed as an external constant according to a dilute fluid at gas-exchange equilibrium with an assumed $p\text{O}_2$ value, given a Henry's Law constant of $1.41 \times 10^{-3} \text{ M atm}^{-1}$ (appropriate for a temperature of 20°C ; 70).

The second formulation, meant to represent surface-catalyzed abiotic Mn(II) oxidation, is depicted according to (71, 72):

$$-\frac{d[\text{Mn(II)}]}{dt} = \frac{d[\text{MnO}_x]}{dt} = [\text{Mn(II)}][\text{OH}^-]^2[\text{O}_2](k_{hom} + k_{het}[\text{MeO}_x]\{\text{SOH}\}) ,$$

where, in addition to the terms described above, k_{hom} represents a rate constant for homogeneous Mn(II) oxidation from solution, k_{het} represents a rate constant for heterogeneous reaction of Mn(II) on oxide surfaces, $[\text{MeO}_x]$ represents the concentration of metal oxide, $\{\text{SOH}\}$ represents the metal oxide surface site density, and $[\text{OH}^-]$ essentially prescribes the control of ambient pH on reaction speed.

For the abiotic rate calculations, we assume a soil porosity of 0.3, a total Fe content of 5.04 wt% (73) and a reactive Fe fraction ranging between 0.25-0.50, based on analysis of modern riverine particulates (74). We assume a range for specific surface area ($300\text{-}600 \text{ m}^2 \text{ g}^{-1}$) and surface OH site density (20 nm^{-2}) typical for ferrihydrite or $\text{Fe}_2\text{O}_3 \cdot \text{H}_2\text{O}$ (75-77) yielding a range for $\{\text{SOH}\}$ of $\sim 0.9 - 2 \times 10^{-2} \text{ mol g}^{-1}$. We assume an initial Mn(II) concentration of 100 nM, at the low end of relatively oxidizing riverine (78), estuarine (79, 80) and coastal marine environments not influenced by significant benthic Mn(II) fluxes (e.g., 81). Parameter values and ranges for all calculations are shown in Table S1. We stress that in all cases parameter values were chosen in an effort to remain conservative for our purposes—i.e., in an effort to falsify our interpretation that atmospheric O_2 levels were very low.

The calculations shown in Main Text Fig. 4 depict rates of Cr(III) mobilization as catalyzed by low-affinity microbial Mn(II) oxidation. Given that relatively low-affinity

enzyme kinetics are consistent with stable but limited substrate availability (e.g., 82), we consider it plausible that this would be realistic for bacterial Mn(II) oxidation in a soil system generally. However, it is important to point out that some strains of Mn(II) oxidizing bacteria are capable of catalyzing Mn redox transformations much more rapidly at considerably lower $[O_2]$ levels (Table S1 and Fig. S3). The calculations presented in Main Text Fig. 4 should thus be considered conservative from the perspective of Cr mobilization as driven by biotic Mn redox cycling.

The above rate law for Cr(III) oxidation (i.e., at the expense of a manganite phase) has been employed primarily in an attempt to most accurately represent the importance of Mn(III) in the process of Cr(III) oxidation (83-87). In addition, this rate law has been validated over a relatively wide pH range, making it suitable for analysis of generalized soil fluid conditions. Solid Mn(III) phases are often produced as the initial reactive phase during Mn(II) oxidation, through both biotic (88) and abiotic (89, 90) pathways, and will also form rapidly as surface alteration products during the interaction between newly formed Fe/Mn oxide phases and dissolved Mn(II) (e.g., 91). Indeed, in many natural environments the ultimate production and stabilization of Mn(IV) oxides occurs through the aging of previously formed Mn(III) oxyhydroxides (92).

However, though dissolved Mn(III) species have been shown to be important reactive intermediates in the process of microbial Mn(II) oxidation (93, 94) and have recently been shown to be extremely important electron transfer agents in natural environments (95, 96), it is not yet clear whether such soluble Mn(III) species themselves are capable of inducing Cr(III) oxidation. In addition, in many cases there is evidence against the formation of solid Mn(III) phases during microbial oxidation of Mn(II) in the laboratory (97-99), except at extremely high dissolved Mn(II) levels (98, 100). As a result, we also compute fractional Cr(III) mobilization using kinetic rate data for δ -MnO₂ (birnessite; 85), a commonly observed end product of biological Mn(II) oxidation in laboratory experiments (e.g., 101), and for “hydrous manganese oxide” (HMO; 65).

Rates of Cr(III) oxidation at a given set of accessory parameters using kinetic data for δ -MnO₂ are slower than those associated with γ -MnOOH, while those for HMO are significantly more rapid (Fig. S3). However, utilization of slightly more high affinity enzyme kinetic parameters still results in significant Cr(III) mobilization with δ -MnO₂ (Fig. S3). In addition, none of our calculations accounts for the enhancement of Cr(III) oxidation through the activity of Mn(II) oxidizing bacteria (102), which have been shown to accelerate Cr(III) oxidation relative to rates attainable with synthetic δ -MnO₂ (103).

Rates of Cr(III) mobilization as driven by abiotic heterogeneous Mn(II) oxidation are shown in Fig. S4. As expected, rates of this process are strongly dependent on ambient pH. However, it is also clear that at circumneutral pH abiotic Mn(II) oxidation is sufficiently rapid to fuel significant consumption of Cr(III) on timescales relevant to soil processes (Fig. S4), even at pO_2 levels considered to be limiting for early metazoans. We consider an absence of bacterial catalysis of Mn(II) oxidation prior to the Neoproterozoic very unlikely, given evidence for this process in the Archean (e.g., 37) and the likelihood that dispersal dynamics and lateral gene transfer on geologic timescales would result in

some strains evolving to utilize the same substrates in terrestrial settings. However, it is clear from these calculations that even surface-catalyzed Mn(II) oxidation is in principle capable of driving significant Cr(III) oxidation at remarkably low pO_2 levels. We thus conclude that under a very wide range of environmentally relevant conditions (pH, biotic/abiotic catalysis, Mn(III,IV) phase, metabolic status) significant Cr(III) mobilization can be expected at pO_2 values at and possibly well below those theoretically derived to be inhibitory for metazoan metabolism.

Alternative mechanisms for preserving igneous $\delta^{53}\text{Cr}$ values in marine sediments despite extensive oxidative Cr cycling in terrestrial systems:

One can imagine a range of scenarios in which it is possible to preserve $\delta^{53}\text{Cr}$ values that are the same as primary igneous values in marine Fe-rich sedimentary rocks with authigenic Cr enrichments, despite the presence of an active terrestrial Cr redox cycle. We outline four such scenarios below, and discuss how our samples were selected and characterized to minimize the likelihood of false negative signals for inhibited terrestrial Cr redox cycling.

Detrital Cr Overprint

Most Cr in sedimentary rocks is hosted by detrital Cr phases, many of which are Cr-rich primary igneous phases. This detrital Cr is likely to be characterized by near-zero $\delta^{53}\text{Cr}$ values. Sediment geochemistry and provenance data can provide a measure of how much detrital Cr is present in a sample. Samples with a predominantly detrital Cr source should have Cr/Ti or Cr/Al ratios that are close to shale composites and estimates for the upper continental crust. Many of our samples contain Cr/Ti ratios well above crustal composite values, indicating authigenic Cr enrichment (Main Text Fig. 2). Critically, however, in Phanerozoic samples we observe a strong relationship between the amount of authigenic Cr in a sample and its Cr isotope ratio. This observation shows that admixtures of detrital Cr phases can and do impact the isotopic composition of ironstones and other iron-rich sedimentary lithologies, and is to first-order responsible for controlling the variance observed in the Phanerozoic Cr isotope record. Further, a number of observations from *in situ* LA-ICP-MS and microprobe work provide support for this conceptual model of mixing detrital Cr with authigenic Cr: (1) There is significant authigenic Cr within iron oxide clasts; and (2) regions of unusual Cr enrichment within detrital (Fe-poor) grains are observed, but are rare (Fig. S5). This implies that Cr(VI) and/or Cr(III) was scavenged and incorporated into sedimentary grains, and samples with high authigenic Cr contents would record large Cr isotope fractionations from bulk silicate Earth if they were present in the weathering environment at that time. As discussed in the Main Text, we hypothesize that this Cr was sourced primarily by environmentally mobile Cr(III) removed through flocculation and scavenging in nearshore marine environments where many ironstones are inferred to have formed (see above).

Local Hydrothermal Overprint

Though their role is poorly constrained at present, it is possible that high- or low-temperature hydrothermal systems may provide a non-trivial source of Cr to marine systems. Given the initial source for such a flux (e.g., primary igneous Cr hosted in

basaltic ocean crust) and the relatively elevated temperatures that would be associated with Cr mobilization, it is a reasonable null hypothesis that Cr introduced by hydrothermal systems would have an isotopic composition similar to primary igneous values. If correct, hydrothermal processes present two possible mechanisms for generating false positives—one that operates on a local scale (discussed here) and one global in scope (discussed below). On a regional/basinal scale, a marine sedimentary system proximal to a zone of significant hydrothermal discharge would be expected to show authigenic Cr enrichment (e.g., elevated Cr/Ti or Cr/Al ratios) and near-zero $\delta^{53}\text{Cr}$ values. We expect that hydrothermally sourced Cr in marine systems will be largely scavenged in the proximity hydrothermal center given sparse Cr(III) solubility at a neutral to alkaline pH. However, if hydrothermal Cr(III) becomes ligand bound it may be possible to have greater Cr(III) mobility. Our mid-Proterozoic and Phanerozoic samples are in all cases from shallow, high-energy depositional settings without any geological indication of nearby hydrothermal activity (aside from earlier hypotheses to source the Fe for these lithotypes). We therefore consider this scenario to be an unlikely explanation for the pattern seen in this particular sample set. That said, though samples from the Pongola Supergroup were deposited in an epicontinental setting it is not possible to rule out hydrothermal activity for this Archean environment (37).

Diagenetic/Metamorphic Overprint

Authigenic Cr from early/late diagenetic or metamorphic fluids would be expected to result in a range of Cr enrichment and $\delta^{53}\text{Cr}$ patterns, depending on the source Cr for the alteration fluid and the time/temperature history of the Cr mobilization process. However, some subset of these processes could yield a sedimentary rock with authigenic Cr enrichment (e.g., elevated Cr/Ti or Cr/Al ratios) and near-zero $\delta^{53}\text{Cr}$ values. In principle, this can occur in any sedimentary rock type and fabric, but is likely to be especially significant in rocks with very low initial Cr concentrations that are known to commonly experience extensive recrystallization, as is often the case in carbonates. In addition, such an overprint will be most likely if reducing post-depositional fluids are introduced that have scavenged Cr from rocks with igneous $\delta^{53}\text{Cr}$ compositions—requirements often met by high-temperature metamorphic fluids. The Cr in our samples is found predominantly in syndepositional authigenic hematite—within textures that typically display limited recrystallization relative to surrounding cements (e.g., Fig. S1). This Cr distribution is consistent with scavenging of riverine and/or seawater Cr but is more difficult to explain through later introduction by diagenetic/metamorphic fluids. In addition, our focus is on oxide-facies Fe-rich chemical sediments, and the current redox character of the sediments makes it unlikely that reducing Cr(III)-rich fluids have significantly altered primary geochemical signals. Indeed, we would expect that alteration via oxidizing fluids (containing Cr(VI) as CrO_4^{2-} and HCrO_4^- species) would yield predominantly positive $\delta^{53}\text{Cr}$ values and thus, if anything, a false positive signal for terrestrial Cr cycling.

Partial Reduction Overprint

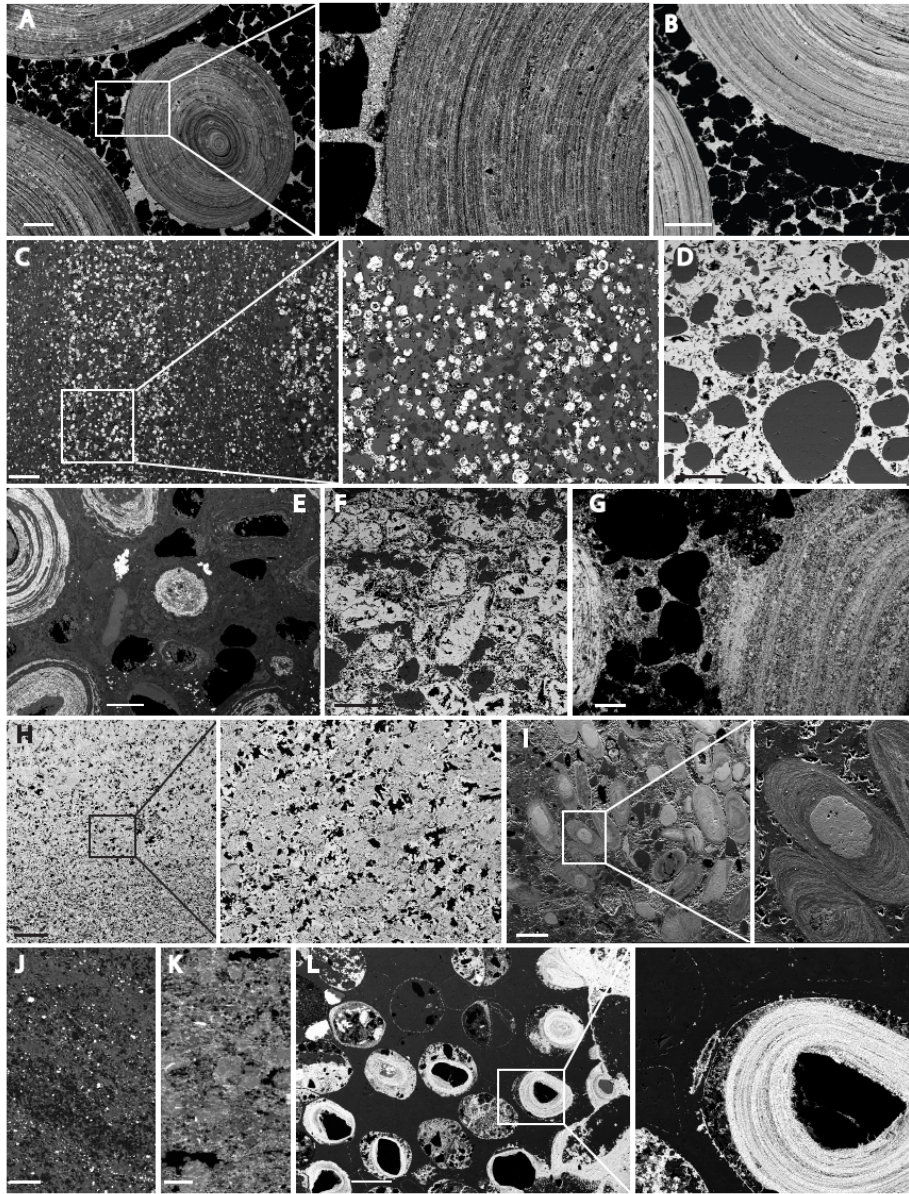
Because of the large ^{52}Cr enrichments expected in the products of partial Cr(VI) reduction, it is possible that near-zero $\delta^{53}\text{Cr}$ values in Fe-rich chemical sediments could result from partial reduction of a contemporaneous Cr(VI) pool that was ^{53}Cr -enriched—

and thus overprint the isotopic effects of vigorous oxidative Earth surface Cr cycling. However, there is significant variability in the fractionations observed with partial Cr(VI) reduction and sediment $\delta^{53}\text{Cr}$ values will range broadly as a function of the extent of reduction and scavenging. As a result, sedimentary systems where Cr enrichment is linked to partial Cr(VI) reduction should be characterized by notable $\delta^{53}\text{Cr}$ variability. For example, a relatively large range of $\delta^{53}\text{Cr}$ within a single unit (such as the Neoproterozoic Wynniatt Formation) may be linked to variable removal during partial Cr(VI) reduction, but this process is an extremely unlikely explanation for the constant near zero values observed in mid-Proterozoic ironstones. The latter would require that in all instances the effective fractionation factor for Cr removal into sediments was offset from a (presumably heavy) seawater value by the requisite amount to yield near-zero $\delta^{53}\text{Cr}$ values. In essence, this would imply either a single uniform Cr(VI) reduction process (e.g., reductant species and fractionation factor) combined with constant fractional removal in all of the examined systems (in addition to a seawater Cr pool that was isotopically homogeneous over timescales greatly in excess of the modern marine residence time of Cr) or serial combination of a range of Cr(VI) reduction processes and fractional Cr(VI) removal values that would result in effective fractionation perfectly offset from changing seawater values to yield values within the igneous range. Both of these scenarios are extremely unlikely.

Decoupling Between Atmospheric $p\text{O}_2$ and Soil Fluid Redox

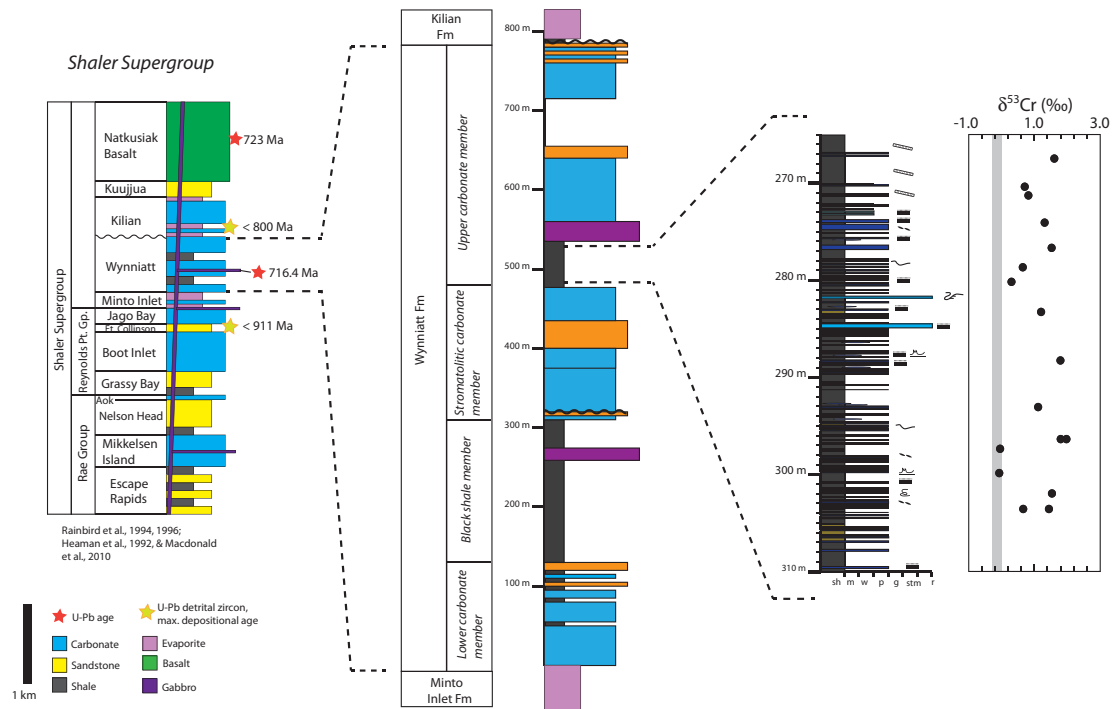
Modern soil and groundwaters are commonly anaerobic despite extremely high atmospheric $p\text{O}_2$ levels. This is the result of sedimentary respiration of organic matter associated with a pervasive and active terrestrial biosphere. Thus, it is possible to imagine a scenario in which weathering environments are partially decoupled from atmospheric $p\text{O}_2$ such that reducing conditions within soil fluids inhibit Mn oxidation despite high $p\text{O}_2$ —in effect decoupling the surface $\delta^{53}\text{Cr}$ signal from atmospheric O_2 levels. However, there appears to be no obvious secular change in Cr isotope composition of ironstones associated with the terrestrialization of Earth's surface suggesting that the most obvious mechanism for both decoupling surface fluid redox from atmospheric $p\text{O}_2$ and changing surface fluid pH has had a minimal effect on the basic isotopic contrast between mid-Proterozoic and Phanerozoic nearshore Fe-rich chemical sediments. In addition, the isotopic shift we observe is the opposite of what would be expected in both cases, with cycling of terrestrial biomass on a large scale providing a ready source of reductant and a flux of proton equivalents into surface fluids through the combined effects of organic acid production and CO_2 pumping. Similarly, localized marine and terrestrial environments can, in theory, become enriched in O_2 (e.g., 104). Therefore, signals for oxidative processes may not reflect background surface redox conditions—e.g., the environmental state that is shaping broad-scale environmental selective pressures. As such, evidence for strongly oxidizing Proterozoic marine systems is not inconsistent with evidence for inhibited coupled Cr-Mn oxidation in terrestrial systems.

Figure S1:



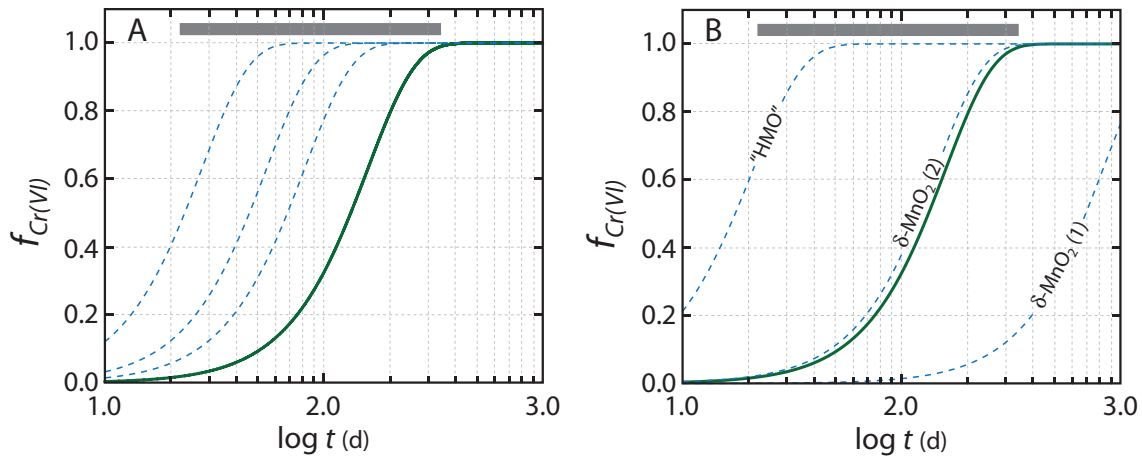
SEM photomicrographs of representative ironstone samples. (A) Sherwin Formation with finely laminated hematitic ooids and a coarser hematite cement. (B) Sherwin Formation with finely laminated hematitic ooids and massive hematite cement around quartz sand grains. (C) Chuanlinggou Formation with fine sand-sized hematite grains in a silt and sand matrix. (D) Chuanlinggou Formation with hematite cement surrounding quartz sand grains. (E) Chuanlinggou Formation with iron oxides ooids (dull white), iron carbonate ooids (dull grey) and rare iron sulfides (bright white). This is the only facies with significant sulfide phases. (F) Chuanlinggou Formation with non-coated hematite grains and quartz sand grains surrounded by hematite cements. (G) Chuanlinggou Formation with laminated hematitic ooids and a hematite cement around quartz sand grains. (H) Aok Formation fine sand hematite granules with surrounding hematite and chert cement. (I) Frodingham Ironstone with chamosite ooids in a mudstone and silt matrix. (J) Freedom Formation with the hematite grains (bright white) in a silt and mudstone matrix. (K) Freedom Formation with hematite grains and a predominantly quartz matrix. (L) Red Mountain Formation hematite ooids and quartz sand grains with quartz cements.

Figure S2:



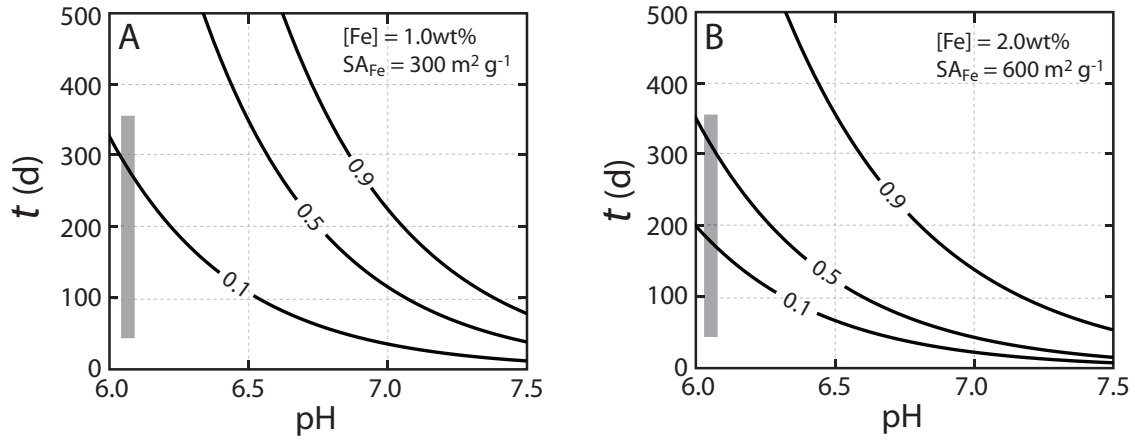
Stratigraphic context for the Wynniatt Formation Cr isotope data. Shown at far left is a simplified stratigraphic section of the Shaler Supergroup, with absolute age constraints as given. Middle panel shows a more detailed section through the Wynniatt Formation, with the section examined here further expanded in the right panel. The grey bar in the far right panel shows the igneous range ($-0.12 \pm 0.101\text{‰}$; 1σ). External reproducibility on Cr isotope data (2σ) is smaller than the symbol size.

Figure S3:



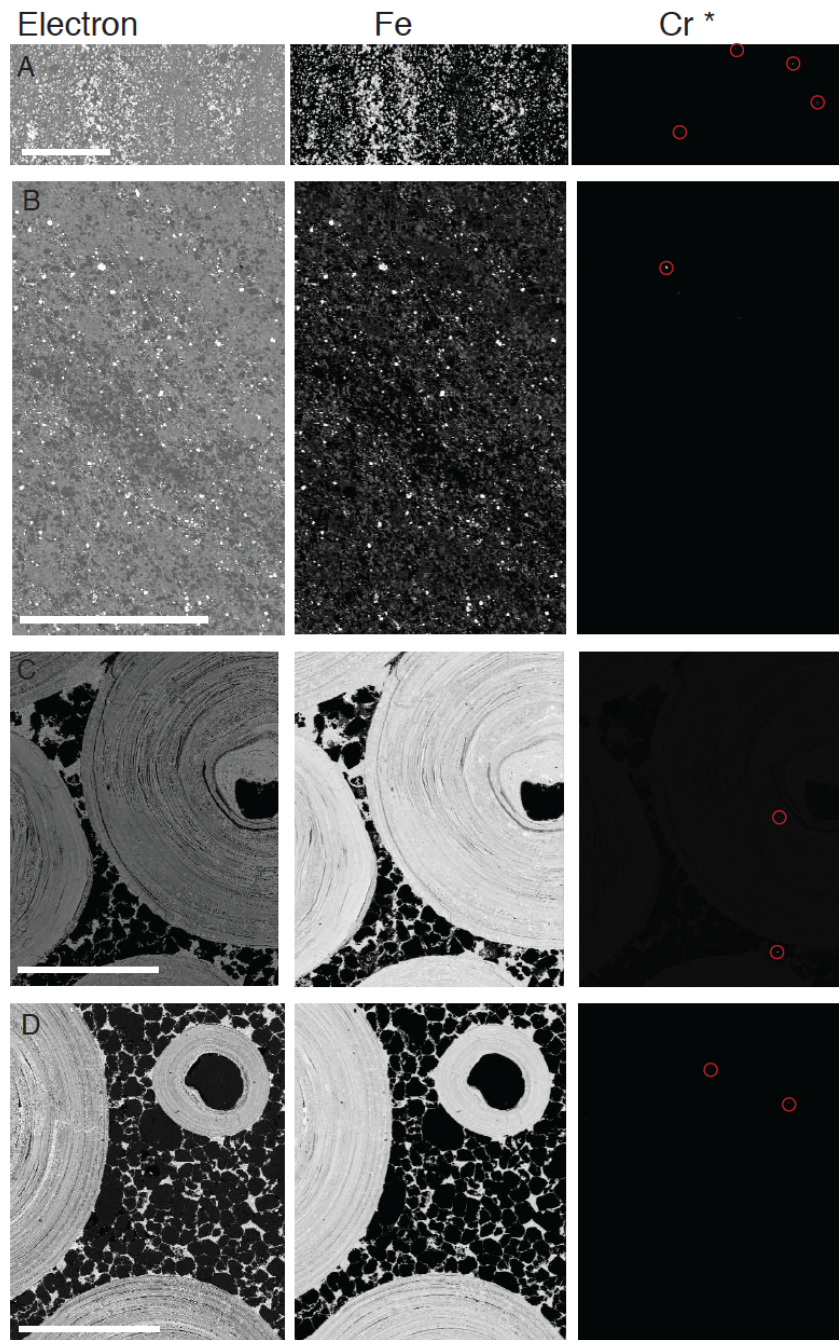
Sensitivity analysis of models that employ biotic Mn(II) oxidation. Shown (A) are the effects of utilizing higher affinity enzyme kinetics (i.e., higher μ_{max} , lower K_{O_2}) (blue dashed curves) in comparison to the baseline case (solid green curve). Shown in (B) are the effects of using rate laws for a range of Mn(III,IV) phases. Blue dashed curves correspond to calculations using kinetic parameters for hydrous manganese oxides ("HMO"; 65) and birnessite ($\delta\text{-MnO}_2$; 85) using baseline enzyme kinetics [$\delta\text{-MnO}_2(1)$] and more moderate values [$\mu_{max} = 14 \text{ nM h}^{-1}$, $K_{O_2} = 0.87 \text{ } \mu\text{M}$; $\delta\text{-MnO}_2(2)$]. The solid green curve in both panels is the baseline case, and the grey bar is as described in the main text. All calculations are performed at the theoretical threshold for a bilaterian with a circulatory system (3).

Figure S4:



Results from models that employ abiotic surface-catalyzed Mn(II) oxidation. Shown in both (A) and (B) are timescales of oxidative Cr(III) mobilization as a function of pH for a range of fractional conversions of Cr(III) to Cr(VI) (contour labels). The rate constant used for Cr(III) oxidation with γ -MnOOH is $1.0 \times 10^{-3} \text{ L m}^{-2} \text{ s}^{-1}$ (see text). Calculations shown in (A) assume a smaller reactive Fe budget and reactive surface area for Fe oxides than those depicted in (B). The grey bars are as in Fig. 4 and Fig. S3. All calculations are performed at the theoretical threshold for a bilaterian with a circulatory system (3).

Figure S5:



Wavelength-dispersive spectroscopy on X-rays emitted during electron microprobe analysis. enables us to gauge the extent of Cr enriched grains present in our samples. Qualitative maps of backscattered electrons, Fe, and Cr are shown left to right as grayscale intensities. Cr* reflects all pixels with $c s^{-1} > 350$ (roughly 3 standard deviations beyond the mean) and reveals the presence of Cr concentrated regions. For clarity these small domains are highlighted by red circles. All scale bars are 1000 microns.

Table S1:

Parameter	Value	Units	Source
μ_{max}	3.6 – 16	nM h ⁻¹	(82, 105)
K_{O_2}	0.87 – 10.5	μ M	(82, 105)
k_{hom}	4 x 10 ¹²	M ⁻³ d ⁻¹	(71, 72)
k_{het}	1 x 10 ¹⁸	M ⁻⁴ d ⁻¹	(69, 81, 106)
k_*	0.5 – 1.0 x 10 ⁻³	L m ⁻² s ⁻¹	(63)
[FeO _x]	1.0 – 2.0	wt%	[see text]
[Mn(II)]	10 ⁻⁷	mol L ⁻¹	[see text]
SA _{Mn}	10 – 100	m ² g ⁻¹	
SA _{Fe} (abiotic)	300 – 600	m ² g ⁻¹	[see text]
porosity	0.3	-	
[Cr] _{parent}	200	μ g g ⁻¹	[see text]
K_H	1.41 x 10 ⁻³	M atm ⁻¹	(70)

Parameter values for kinetic calculations. For parameter values that are reported as ranges, the calculations presented in Main Text Fig. 3 utilize the most conservative values – i.e., values that yield the lowest rates of Mn(II)-Cr(III) oxidation.

Database S1 (separate file)

Sample and geochemical information.

Database S2 (separate file)

Laser Ablation data. Gray bars indicate data from cements.

References:

1. N. J. Butterfield, Oxygen, animals and oceanic ventilation: an alternative view. *Geobiology* **7**, 1 (2009).
2. D. H. Erwin et al., The Cambrian Conundrum: Early Divergence and Later Ecological Success in the Early History of Animals. *Science* **334**, 1091 (2011).
3. E. A. Sperling, G. P. Halverson, A. H. Knoll, F. A. Macdonald, D. T. Johnston, A basin redox transect at the dawn of animal life. *Earth and Planetary Science Letters* **371**, 143 (2013).
4. D.B. Mills, Ward LM, Jones C, Sweeten B, et al. 2014. Oxygen requirements of the earliest animals. *Proceedings of the National Academy of Sciences of the United States of America* **111**: 4168-72.
5. J. L. Payne et al., The evolutionary consequences of oxygenic photosynthesis: a body size perspective. *Photosynthesis Research* **107**, 37 (2011).
6. H. D. Holland, The oxygenation of the atmosphere and oceans. *Philosophical Transactions of the Royal Society B* **361**, 903 (2006).
7. R. Rye, H. D. Holland, *Paleosols and the evolution of atmospheric oxygen: a critical review*. *American Journal of Science* **298**, 621 (1998).
8. D. E. Canfield, The early history of atmospheric oxygen: Homage to Robert M. Garrels. *Annual Reviews of Earth and Planetary Sciences* **33**, 1 (2005).
9. L. Kump, The rise of atmospheric oxygen. *Nature* **451**, 277 (2008).
10. R. Frei, C. Gaucher, S. W. Poulton, D. E. Canfield, Fluctuations in Precambrian atmospheric oxygenation recorded by chromium isotopes. *Nature* **461**, 250 (2009).
11. A. S. Ellis, T. M. Johnson, T. D. Bullen, Using chromium stable isotope ratios to quantify Cr(VI) reduction: Lack of sorption effects. *Environmental Science & Technology* **38**, 3604 (2004).
12. T. M. Johnson, T. D. Bullen, Mass-dependent fractionation of selenium and chromium isotopes in low-temperature environments. *Geochemistry of Non-Traditional Stable Isotopes* **55**, 289 (2004).
13. E. A. Schauble, G. R. Rossman, H. P. J. Taylor, Theoretical estimates of equilibrium chromium-isotope fractionations. *Chemical Geology* **205**, 99 (2004).
14. S. Zink, R. Schoenberg, M. Staubwasser, Isotopic fractionation and reaction kinetics between Cr(III) and Cr(VI) in aqueous media *Geochimica et Cosmochimica Acta* **74**, 5729 (2010).
15. R. Bartlett, B. James, Behavior of Chromium in Soils .3. Oxidation. *Journal of Environmental Quality* **8**, 31 (1979).
16. S. E. Fendorf, Surface reactions of chromium in soils and waters. *Geoderma* **67**, 55 (1995).
17. J. Kotas, Z. Stasicka, Chromium occurrence in the environment and methods of its speciation. *Environmental Pollution* **107**, 263 (2000).
18. A. Ellis, T. D. Bullen, J. T.M., Chromium isotopes and the fate of hexavalent chromium in the environment. *Science* **295**, 2060 (2002).
19. R. Schoenberg, S. Zink, M. Staubwasser, F. von Blanckenburg, The stable Cr isotope inventory of solid Earth reservoirs determined by double spike MC-ICP-MS. *Chemical Geology* **249**, 294 (2008).

20. S. A. Crowe et al., Atmospheric oxygenation three billion years ago. *Nature* **501**, 535 (2013).
21. Materials and methods are available on *Science* online.
22. R. C. Aller, J. E. Mackin, R. T. Cox, Diagenesis of Fe and S in Amazon Inner Shelf Muds - Apparent Dominance of Fe Reduction and Implications for the Genesis of Ironstones. *Continental Shelf Research* **6**, 263 (1986).
23. A. C. Brown, Refinements for footwall red-bed diagenesis in the sediment-hosted stratiform copper deposits model. *Economic Geology* **100**, 765 (2005).
24. D. Leach et al., Sediment-hosted lead-zinc deposits: A global perspective. *Economic Geology*, **100**, 561 (2005).
25. C. Reinhard et al., Proterozoic ocean redox and biogeochemical stasis. *Proceedings of the National Academy of Sciences* **110**, 5357 (2013).
26. D. van Acken, D. Thomson, R. H. Rainbird, R. A. Creaser, Constraining the depositional history of the Neoproterozoic Shaler Supergroup, Amundsen Basin, NW Canada: Rhenium-osmium dating of black shales from the Wynniatt and Boot Inlet Formations. *Precambrian Research* **236**, 124 (2013).
27. Full model details are available on *Science* online
28. N. D. Sheldon, Precambrian paleosols and atmospheric CO₂ levels. *Precambrian Research* **147**, 148 (2006).
29. E. A. Zbinden, H. D. Holland, C. R. Feakes, S. K. Dobos, The Sturgeon Falls Paleosol and the Composition of the Atmosphere 1.1 Ga B.P. *Precambrian Research* **42**, 141 (1988).
30. T.W. Lyons, C.T. Reinhard, N.J. Planavsky, The rise of oxygen in Earth's early ocean and atmosphere. *Nature* **506**, 307 (2014).
31. G. D. Love et al., 2008. Fossil steroids record the appearance of Demospongiae during the Cryogenian period. *Nature* **457**, 718 (2008).
32. A.H. Knoll, Paleobiological Perspectives on Early Eukaryotic Evolution Cold Spring Harbor Perspectives on Biology **6**, a016121 (2014).
33. R. R. Large, *et al.* Gold and Trace Element Zonation in Pyrite Using a Laser Imaging Technique: Implications for the Timing of Gold in Orogenic and Carlin-Style Sediment-Hosted Deposits. *Economic Geology* **104**, 635–668 (2009).
34. J. B. Maynard, Geochemistry of Oolitic Iron-Ores, an Electron-Microprobe Study. *Economic Geology* **81**, 1473 (1986).
35. F. B. Van Houten, D. P. Bhattacharyya, Phanerozoic Oolitic Ironstones - Geologic Record and Facies Model. *Annual Review of Earth and Planetary Sciences* **10**, 441 (1982).
36. K. O. Konhauser *et al.*, Aerobic bacterial pyrite oxidation and acid rock drainage during the Great Oxidation Event. *Nature* **478**, 369 (2011).
37. N. J. Planavsky *et al.*, Evidence for oxygenic photosynthesis half a billion years before the Great Oxidation Event. *Nature Geoscience* **7**, 283 (2014).
38. C. T. Reinhard, et al., The isotopic composition of authigenic chromium in anoxic marine sediments: A case study from the Cariaco Basin. *Earth and Planetary Science Letters* (in press).
39. A. Bekker *et al.*, Iron Formation: The Sedimentary Product of a Complex Interplay among Mantle, Tectonic, Oceanic, and Biospheric Processes. *Economic Geology* **105**, 467 (2010).

40. S. N. Lu, Li, H. M. , A precise U–Pb single zircon age determination for the volcanics of the Dahongyu Formation, Changcheng System in Jixian. *Bulletin of the Chinese Academy of Geological Sciences*. **22**, 137 (1991).
41. L. Z. Gao, Zhang, C. H., Yin, C. Y., Shi, X. Y., Wang, Z. Q., Liu, Y. M., Liu, P. J., Tang, F., Song, B. , SHRIMP zircon ages: basis for refining the chronostratigraphic classification of the Meso- and Neoproterozoic strata in North China Old Land. *Acta Geoscientica Sinica* **29**, 366 (2008).
42. H. K. Li, Su, W. B., Zhou, H. Y., Geng, J. Z., Xiang, Z. Q., Cui, Y. R., Liu, W. C., Lu, S. N. , The base age of the Changchengian System at the northern North China Craton should be younger than 1670 Ma: Constraints from zircon U-Pb LA-MC-ICPMS dating of a granite-porphry dike in Miyun County, Beijing. *Earth Science Frontiers* **18**, 108 (2011).
43. P. Peng, Liu, F., Zhai, M. G., Guo, J. H. , Age of the Miyun dyke swarm: constraints on the maximum depositional age of the Changcheng System. *Chinese Science Bulletin* **57**, 105 (2012).
44. L. G. J. Medaris, Singer, B.S., Dott, R.H., Jr., Naymark, A., Johnson, C.M. and Schott, R.C. , Late Paleoproterozoic climate, tectonics and metamorphism in the southern Lake Superior region and Proto-North America: Evidence from Baraboo interval quartzites. *Journal of Geology* **111**, 243 (2003).
45. D. Holm, D. Schneider, C. D. Coath, Age and deformation of Early Proterozoic quartzites in the southern Lake Superior region: Implications for extent of foreland deformation during final assembly of Laurentia. *Geology* **26**, 907 (1998).
46. S. T. Abbott, I. P. Sweet, Tectonic control on third-order sequences in a siliciclastic ramp-style basin: an example from the Roper Superbasin (Mesoproterozoic), northern Australia. *Australian Journal of Earth Sciences* **47**, 637 (2000).
47. M. Jackson, Sweet , IP, Powell, TG Studies on petroleum geology and geochemistry, middle Proterozoic, McArthur Basin Northern Australia I: Petroleum potential. *The APEA Journal* **28**, 283 (1988).
48. M. Kralick, Rb–Sr age determinations on Precambrian carbonate rocks of the Carpentarian McArthur Basin, Northern Territory, Australia. *Precambrian Research* **18**, 157 (1982).
49. R. H. Rainbird, C. W. Jefferson, G. M. Young, The early Neoproterozoic sedimentary succession B of northwestern Laurentia: Correlations and paleogeographic significance. *Geological Society of America Bulletin* **108**, 454 (Apr, 1996).
50. N. M. R. Rayner, RH, U-Pb Geochronology of the Shaler Supergroup, Victoria Island, northwest Canada: 2009-2013. *Geological Survey of Canada Open File 7419*, (2013).
51. L. M. Heaman, A. N. Lecheminant, R. H. Rainbird, Nature and Timing of Franklin Igneous Events, Canada - Implications for a Late Proterozoic Mantle Plume and the Break-up of Laurentia. *Earth and Planetary Science Letters* **109**, 117 (Mar, 1992).

52. D. Thomson, R. H. Rainbird, G. Dix, Architecture of a Neoproterozoic intracratonic carbonate ramp succession: Wynniatt Formation, Amundsen Basin, Arctic Canada. *Sedimentary Geology* **299**, 119 (Jan 15, 2014).
53. H. Elderfield, Chromium speciation in sea water. *Earth and Planetary Science Letters* **9**, 10 (1970).
54. M. Pettine, F. J. Millero, Chromium speciation in seawater: The probable role of hydrogen peroxide. *Limnology and Oceanography* **35**, 730 (1990).
55. D. C. Schroeder, G. F. Lee, Potential transformations of chromium in natural waters. *Water, Air, and Soil Pollution* **4**, 355 (1974).
56. C. H. van der weijden, M. Reith, Chromium(III) - chromium(VI) interconversions in seawater. *Marine Chemistry* **11**, 565 (1982).
57. S. E. Fendorf, R. J. Zasoski, Chromium(III) oxidation by delta-MnO₂. 1. Characterization. *Environmental Science & Technology* **26**, 79 (1992).
58. D. Banerjee, H. W. Nesbitt, Oxidation of aqueous Cr(III) at birnessite surfaces: Constraints on reaction mechanism. *Geochimica et Cosmochimica Acta* **63**, 1671 (1999).
59. J. G. Kim, J. B. Dixon, C. C. Chusuei, Y. J. Deng, Oxidation of chromium(III) to (VI) by manganese oxides. *Soil Science Society of America Journal* **66**, (2002).
60. R. M. Weaver, M. F. Hochella, The reactivity of seven Mn-oxides with Cr_{aq}⁽³⁺⁾: A comparative analysis of a complex, environmentally important redox reaction. *American Mineralogist* **88**, 2016 (2003).
61. D. Fandeur *et al.*, XANES evidence for oxidation of Cr(III) to Cr(VI) by Mn-oxides in a lateritic regolith developed on serpentinized ultramafic rocks of New Caledonia. *Environmental Science & Technology* **43**, 7384 (2009).
62. L. E. Eary, D. Rai, Kinetics of chromium(III) oxidation to chromium(VI) by reaction with manganese-oxide. *Environmental Science & Technology* **21**, 1187 (1987).
63. C. A. Johnson, A. G. Xyla, The oxidation of chromium(III) to chromium(VI) on the surface of manganite (gamma-MnOOH). *Geochimica et Cosmochimica Acta* **55**, 2861 (1991).
64. E. Silvester, L. Charlet, A. Manceau, Mechanism of chromium(III) oxidation by Na-buserite. *The Journal of Physical Chemistry* **99**, 16662 (1995).
65. G. Landrot, M. Ginder-Vogel, D. L. Sparks, Kinetics of chromium(III) oxidation by manganese(IV) oxides using quick scanning X-ray absorption fine structure spectroscopy (Q-XAFS). *Environmental Science & Technology* **44**, 143 (2010).
66. P. E. Kepkay, Kinetics of microbial manganese oxidation and trace metal binding in sediments: Results from an in situ dialysis technique. *Limnology and Oceanography* **30**, 713 (1985).
67. B. M. Tebo, S. Emerson, Microbial manganese(II) oxidation in the marine-environment—a quantitative study *Biogeochemistry* **2**, 149 (1986).
68. F. C. Boogerd, J. P. M. de Vrind, Manganese oxidation by *Leptothrix discophora*. *Journal of Bacteriology* **169**, 489 (1987).
69. C. A. Johnson, M. Ulrich, L. Sigg, D. M. Imboden, A mathematical model of the manganese cycle in a seasonally anoxic lake. *Limnology and Oceanography* **36**, 1415 (1991).

70. H. E. Garcia, L. I. Gordon, Oxygen solubility in seawater - better fitting equations. *Limnology and Oceanography* **37**, 1307 (1992).
71. S. H. R. Davies, J. J. Morgan, Manganese(II) oxidation kinetics on metal oxide surfaces. *Journal of Colloid and Interface Science* **129**, 63 (1989).
72. P. J. von Langen, K. S. Johnson, K. H. Coale, V. A. Elrod, Oxidation kinetics of manganese (II) in seawater at nanomolar concentrations. *Geochimica et Cosmochimica Acta* **61**, 4945 (1997).
73. R. L. Rudnick, S. Gao, in *Treatise on Geochemistry*, H. D. Holland, K. K. Turekian, Eds. (Elsevier, Oxford, 2003), vol. 6, pp. 1-64.
74. S. W. Poulton, R. Raiswell, The low-temperature geochemical cycle of iron: From continental fluxes to marine sediment deposition. *American Journal of Science* **302**, 774 (2002).
75. C. C. Fuller, J. A. Davis, G. A. Waychunas, Surface chemistry of ferrihydrite: Part 2. Kinetics of arsenate adsorption and coprecipitation. *Geochimica et Cosmochimica Acta* **57**, 2271 (1993).
76. T. D. Waite, J. A. Davis, T. E. Payne, G. A. Waychunas, N. Xu, Uranium(VI) adsorption to ferrihydrite: Application of a surface complexation model. *Geochimica et Cosmochimica Acta* **58**, 5465 (1994).
77. T. Hiemstra, W. H. Van Riemsdijk, A surface structural model for ferrihydrite I: Sites related to primary charge, molar mass, and mass density. *Geochimica et Cosmochimica Acta* **73**, 4423 (2009).
78. C. Pontér, J. Ingri, K. Boström, Geochemistry of manganese in the Kalix River, northern Sweden. *Geochimica et Cosmochimica Acta* **56**, 1485 (1992).
79. M. Yang, S. A. Sañudo-Wilhelmy, Cadmium and manganese distributions in the Hudson River estuary: interannual and seasonal variability. *Earth and Planetary Science Letters* **160**, 403 (1998).
80. J. S. Roitz, A. R. Flegal, K. W. Bruland, The biogeochemical cycling of manganese in San Francisco Bay: Temporal and spatial variability in surface water concentrations. *Estuarine, Coastal and Shelf Science* **54**, 227 (2002).
81. B. Thamdrup, R. N. Glud, J. W. Hansen, Manganese oxidation and in-situ manganese fluxes from a coastal sediment. *Geochimica et Cosmochimica Acta* **58**, 2563 (Jun, 1994).
82. B. G. Clement, G. W. Luther, B. M. Tebo, Rapid, oxygen-dependent microbial Mn(II) oxidation kinetics at sub-micromolar oxygen concentrations in the Black Sea suboxic zone. *Geochimica et Cosmochimica Acta* **73**, 1878 (Apr 1, 2009).
83. M. W. Rophael, S. N. Boulis, Kinetics of the oxidation of chromium(III) ions by trimanganese tetroxide and by manganese(III) oxide. *Surface Technology* **16**, 243 (1982).
84. J. B. Chung, R. J. Zasoski, S. U. Lim, Kinetics of chromium(III) oxidation by various manganese oxides. *Agricultural Chemistry and Biotechnology* **37**, 414 (1994).
85. P. S. Nico, R. J. Zasoski, Importance of Mn(III) availability on the rate of Cr(III) oxidation on delta-MnO₂. *Environmental Science & Technology* **34**, 3363 (2000).
86. R. M. Weaver, M. F. Hochella, E. S. Ilton, Dynamic processes occurring at the Cr_{aq}(III)-manganite (gamma-MnOOH) interface: Simultaneous adsorption,

- microprecipitation, oxidation/reduction, and dissolution. *Geochimica et Cosmochimica Acta* **66**, 4119 (2002).
87. A. B. Chwang *et al.*, Thin film encapsulated flexible organic electroluminescent displays. *Appl Phys Lett* **83**, 413 (Jul 21, 2003).
 88. D. Hastings, S. Emerson, Oxidation of manganese by spores of a marine bacillus: Kinetic and thermodynamic considerations. *Geochimica et Cosmochimica Acta* **50**, 1819 (1986).
 89. J. D. Hem, C. J. Lind, Nonequilibrium models for predicting forms of precipitated manganese oxides. *Geochimica et Cosmochimica Acta* **47**, 2037 (1983).
 90. J. W. Murray, J. G. Dillard, R. Giovanoli, H. Moers, W. Stumm, Oxidation of Mn(II): Initial mineralogy, oxidation state and ageing. *Geochimica et Cosmochimica Acta* **49**, 463 (1985).
 91. J. L. Junta, M. F. Hochella Jr., Manganese (II) oxidation at mineral surfaces: A microscopic and spectroscopic study. *Geochimica et Cosmochimica Acta* **58**, 4985 (1994).
 92. P. Anschutz, K. Dedieu, F. Desmazes, G. Chaillou, Speciation, oxidation state, and reactivity of particulate manganese in marine sediments. *Chemical Geology* **218**, 265 (2005).
 93. S. M. Webb, G. J. Dick, J. R. Bargar, B. M. Tebo, Evidence for the presence of Mn(III) intermediates in the bacterial oxidation of Mn(II). *Proceedings of the National Academy of Sciences* **102**, 5558 (2005).
 94. C. N. Butterfield, A. V. Soldatova, S. W. Lee, T. G. Spiro, B. M. Tebo, Mn(II,III) oxidation and MnO₂ mineralization by an expressed bacterial multicopper oxidase. *Proceedings of the National Academy of Sciences* **29**, 11731 (2013).
 95. R. E. Trouwborst, B. G. Clement, B. M. Tebo, B. T. Glazer, G. W. Luther, Soluble Mn(III) in suboxic zones. *Science* **313**, 1955 (2006).
 96. A. S. Madison, B. M. Tebo, A. Mucci, B. Sundby, G. W. Luther III, Abundant porewater Mn(III) is a major component of the sedimentary redox system. *Science* **341**, 875 (2013).
 97. K. W. Mandernack, M. L. Fogel, B. M. Tebo, A. Usui, Oxygen isotope analyses of chemically and microbially produced manganese oxides and manganates. *Geochimica et Cosmochimica Acta* **59**, 4409 (1995).
 98. K. W. Mandernack, J. Post, B. M. Tebo, Manganese mineral formation by bacterial spores of the marine *Bacillus*, strain SG-1: Evidence for the direct oxidation of Mn(II) to Mn(IV). *Geochimica et Cosmochimica Acta* **59**, 4393 (1995).
 99. J. R. Bargar, B. M. Tebo, J. E. Villinski, In situ characterization of Mn(II) oxidation by spores of the marine *Bacillus* sp. strain SG-1. *Geochimica et Cosmochimica Acta* **64**, 2775 (2000).
 100. K. Pecher *et al.*, Quantitative charge state analysis of manganese biominerals in aqueous suspension using Scanning Transmission X-ray Microscopy (STXM). *Geochimica et Cosmochimica Acta*, (2003).
 101. B. M. Tebo *et al.*, Biogenic manganese oxides: Properties and mechanisms of formation. *Annual Review of Earth and Planetary Sciences* **32**, 287 (2004).

102. K. J. Murray, M. L. Mozafarzadeh, B. M. Tebo, Cr(III) oxidation and Cr toxicity in cultures of the manganese(II)-oxidizing *Pseudomonas putida* strain GB-1. *Geomicrobiology Journal* **22**, 151 (2005).
103. K. J. Murray, B. M. Tebo, Cr(III) is indirectly oxidized by the Mn(II)-oxidizing bacterium *Bacillus* sp strain SG-1. *Environmental Science & Technology* **41**, 528 (2007).
104. C.T. Reinhard, S.V. LaLonde, T.W. Lyons, Oxidative sulfide dissolution on the early Earth. *Chemical Geology*, 362, 44 (2013)
105. G. J. Dick *et al.*, Enzymatic microbial Mn(II) oxidation and Mn biooxide production in the Guaymas Basin deep-sea hydrothermal plume. *Geochimica et Cosmochimica Acta* **73**, 6517 (2009).
106. S. Emerson, R. E. Cranston, P. S. Liss, Redox species in a reducing fjord: equilibrium and kinetic considerations. *Deep-Sea Research* **26A**, 859 (1979).